

Giant Magneto-Optical Schafer-Hubert Effect in Two-Dimensional van der Waals Antiferromagnets MPS_3 ($M=Mn, Fe, Ni$)

Ping Yang,^{1,2} Wanxiang Feng,^{1,2,*} Gui-Bin Liu,^{1,2} Guang-Yu Guo,^{3,4} and Yugui Yao^{1,2}

¹Key Laboratory of Advanced Optoelectronic Quantum Architecture and Measurement (MOE),
School of Physics, Beijing Institute of Technology, Beijing 100081, China

²Beijing Key Lab of Nanophotonics and Ultrafine Optoelectronic Systems,
School of Physics, Beijing Institute of Technology, Beijing 100081, China

³Department of Physics and Center for Theoretical Physics, National Taiwan University, Taipei 10617, Taiwan

⁴Physics Division, National Center for Theoretical Sciences, Taipei 10617, Taiwan

(Dated: February 22, 2023)

The recent discovery of long-range magnetic order in atomically thin films has triggered particular interest in two-dimensional (2D) van der Waals (vdW) magnetic materials. In this paper, we perform a systematic theoretical study of the magneto-optical Schafer-Hubert effect (MOSHE) in 2D vdW antiferromagnetic MPS_3 ($M = Mn, Fe, Ni$) with multifold intralayer and interlayer magnetic orders. The formula for evaluating the MOSHE in 2D magnets is derived by considering the influence of a non-magnetic substrate. The MOSHE of monolayer and bilayer MPS_3 are considerably large ($> 2^\circ$), originating from the strong anisotropy of in-plane optical conductivity. The Schafer-Hubert rotation angles are surprisingly insensitive to the orientations of the Neel vector, while the Schafer-Hubert ellipticities are identified to be a good criterion to distinguish different interlayer magnetic orders. Our work establishes a theoretical framework for exploring novel 2D vdW magnets and facilitates the promising applications of the 2D MPS_3 family in antiferromagnetic nanophotonic devices.

INTRODUCTION

Two-dimensional (2D) van der Waals (vdW) magnetic materials have attracted emerging attention since the discovery of intrinsically long-range ferromagnetic (FM) order in $Cr_2Ge_2Te_6$ and CrI_3 atomic layers [1, 2]. The highly tunable magnetism and other exciting physical properties by electric gating [3] and strain engineering [4, 5] offer them a promising potential for applications in magnetic sensor, storage, and spintronics. Magneto-optical spectroscopy is a powerful non-contact technique for investigating 2D magnetic materials. For 2D ferromagnets, magneto-optical Kerr effect (MOKE) signals a solid evidence of long-range FM order even down to monolayer limit [2]. Furthermore, first-principles calculations of MOKE in thin films [6, 7] provide a complementary avenue to characterize 2D FM materials [8–11]. For 2D antiferromagnets that have zero net magnetization, the MOKE as a first-order effect is vanishing, and therefore the commonly used magneto-optical techniques are based on second-order effects. [12–14] One option is to probe the difference in absorption or reflectivity for linearly polarized lights parallel and perpendicular to the Neel vector, which is known as magnetic linear dichroism (MLD). Another option is to probe the polarization rotation upon transmission and reflection, which are called magneto-optical Voigt effect [15] and magneto-optical Schafer-Hubert effect (MOSHE) [16], respectively. Since the second-order magneto-optical effects in magnetic materials are usually very weak, the characterization of 2D AFM order has long been considered extremely challenging.

Transition metal thiophosphates MPS_3 ($M = Mn, Fe, Ni$) are a representative family of 2D vdW materials that host multifold intrinsically intralayer AFM orders [17–19]. In a recent

experiment, Zhang et al. [20] observed large MLD in $FePS_3$ with zigzag-AFM order. The large magneto-optical signals enable the detection of 2D AFM domain orientations [20, 21] and the study of ultrafast spin dynamics [22]. Subsequently, the tuning of MLD in $FePS_3$ was realized by coupling with optical-cavity [23], and the MLD at specific wavelength can be even enhanced to a near-unity (100%) value. Such an optically anisotropic 2D magnetic material is desirable for achieving densely integrated polarization selective devices. To date, most of the reports on large linear dichroism and its tuning for 2D materials have been limited to those with in-plane anisotropic crystal structures, such as black phosphorus [24, 25] and $GeSe$ [26]. By contrast, anisotropic 2D magnetic materials are more promising for the fast field-effect control since the magnetic orders are sensitive to external stimuli, e.g., magnetic [27] and strain [28] fields. These recent advances call for an exploration of more excellent 2D AFM magneto-optical materials, however, theoretical studies on the second-order magneto-optical effects in thin films remain absent yet.

In this work, we systematically investigate a representative second-order magneto-optical effect, MOSHE, in 2D vdW AFM MPS_3 using first-principles calculation together with magnetic group analysis. A theoretical formula for evaluating the MOSHE in 2D magnetic materials placed on a non-magnetic substrate is derived for the first time. The MOSHE in $FePS_3$ and $NiPS_3$ with the zigzag-AFM order are close to or even exceed to the magnitudes of first-order magneto-optical effects in conventional ferromagnets, especially the Schafer-Hubert (SH) rotation angle in bilayer $NiPS_3$ records up to 2.4° . We also find that the MOSHE is insensitive to the magnetization direction, and the SH ellipticity can be used to identify interlayer magnetic structures. Our work deepens the understanding of MOSHE in 2D antiferromagnets and facilitate further exploration of novel AFM magneto-optical devices.

* wxfeng@bit.edu.cn

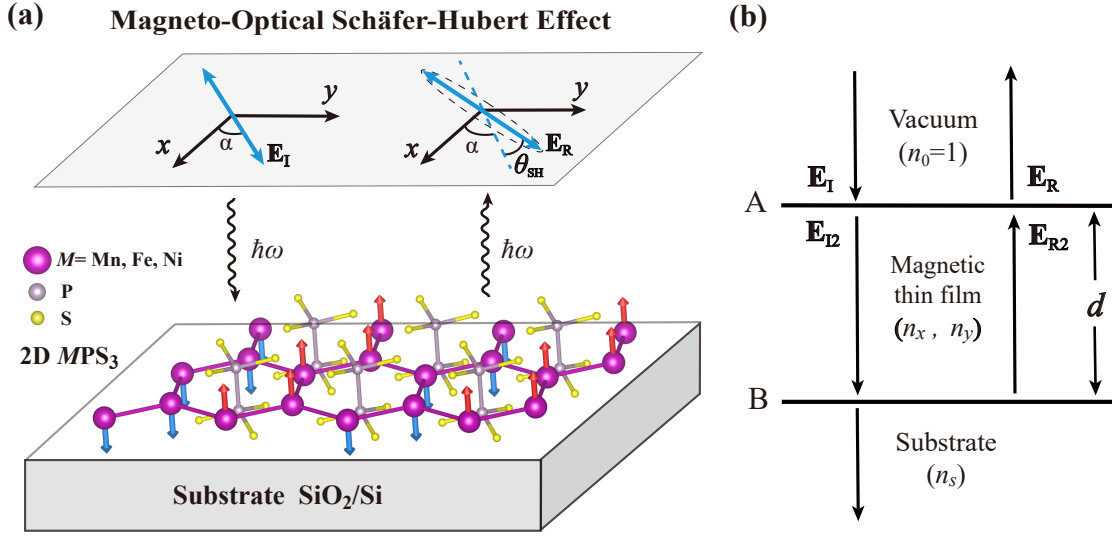


FIG. 1. (a) Schematic illustration of magneto-optical Schärer-Hubert effect emerged in 2D antiferromagnets MPS_3 ($M = \text{Mn, Fe, Ni}$) prepared on SiO_2/Si substrate. The incident light is linearly polarized with the electric field (\mathbf{E}_I) orienting an angle of α from the optically anisotropic axis (here, x -axis). The reflected light becomes elliptically polarized and the polarization plane (\mathbf{E}_R) deflects an angle of θ_{SH} with respect to incident light (\mathbf{E}_I). (b) Optical paths in a magnetic thin film placed on an optically isotropic non-magnetic substrate. Refractive indices (n_0, n_x, n_y, n_s) in each region and the electric fields ($\mathbf{E}_I, \mathbf{E}_{I2}, \mathbf{E}_R, \mathbf{E}_{R2}$) at the interface A are labeled, and d denotes the thickness of magnetic thin film.

RESULTS AND DISCUSSION

When a linearly polarized light normally shines (e.g., along the z -axis) on a thin film with in-plane magnetic anisotropy, the light propagating in the magnetic thin film can be decomposed into two polarized components along orthogonal anisotropic axes with different refractive indices (n_x, n_y) and reflectivity (r_x, r_y). The reflected light would become elliptically polarized accompanied by a rotation of polarization plane with respect to the incident light, namely the MOSHE (Fig. 1a). If the electric field of incident light (\mathbf{E}_I) places at an angle of $\alpha = 45^\circ$ from the x -axis, the SH rotation angle (θ_{SH}) and ellipticity (ψ_{SH}) reach up to their maximums, given by [29]

$$\begin{aligned} \theta_{\text{SH}} &= \frac{1}{2} \text{atan} \left(\frac{2 \text{Re} \chi}{1 - |\chi|^2} \right) - \frac{\pi}{4}, \\ \psi_{\text{SH}} &= \frac{1}{2} \text{asin} \left(\frac{2 \text{Im} \chi}{1 + |\chi|^2} \right), \end{aligned} \quad (1)$$

where $\chi = r_y/r_x$. The reflectivity of a magnetic thin film at the interface A (Fig. 1b) can be written as

$$r_{x(y)} = \frac{n_0 - \tilde{n}_{x(y)}}{n_0 + \tilde{n}_{x(y)}}. \quad (2)$$

Here, $n_0 = 1$ is the refractive index of vacuum, $\tilde{n}_{x(y)}$ is the effective refractive index of a magnetic thin film by considering the influence of its substrate,

$$\tilde{n}_{x(y)} = \frac{1 - r'_{x(y)} \beta_{x(y)}}{1 + r'_{x(y)} \beta_{x(y)}} n_{x(y)}, \quad (3)$$

in which $\beta_{x(y)} = \exp(2i\omega d n_{x(y)}/c)$ with the light frequency ω , light speed c , and film thickness d . The reflectivity of sub-

strate at the interface B is $r'_{x(y)} = (n_{x(y)} - n_s)/(n_{x(y)} + n_s)$ and n_s is the refractive index of substrate. Plugging Eqs. (2) and (3) into Eq. (1), the complex SH angle can be recast as

$$\theta_{\text{SH}} + i\psi_{\text{SH}} \approx \frac{\tilde{n}_x - \tilde{n}_y}{1 - \tilde{n}_x \tilde{n}_y}. \quad (4)$$

For monolayer and few-layer of 2D materials whose thicknesses are far less than the wavelength of visible light (λ), the effective refractive index can be approximated to $\tilde{n}_{x(y)} \approx n_s - i \cdot 2\pi d(n_{x(y)}^2 - n_s^2)/\lambda$. In the case of conventional MOSHE induced by in-plane magnetization (e.g., along the x -axis), the refractive indices by solving the Fresnel equation are given by $n_x = \sqrt{\epsilon_{xx}}$, $n_y = \sqrt{\epsilon_{yy} + \epsilon_{yz}^2/\epsilon_{zz}}$, in which $\epsilon_{\mu\nu}$ with $\mu, \nu \in \{x, y, z\}$ is the permittivity tensor. Then, the complex SH angle can be simplified to

$$\theta_{\text{SH}} + i\psi_{\text{SH}} \approx \frac{i\omega d}{c(n_s^2 - 1)} (\epsilon_{xx} - \epsilon_{yy} - \frac{\epsilon_{yz}^2}{\epsilon_{zz}}). \quad (5)$$

We find that the complex SH angle can be related to the complex Voigt angle [30] via

$$\theta_{\text{SH}} + i\psi_{\text{SH}} = \frac{2(n_x + n_y)}{1 - n_s^2} (\theta_V - i\psi_V), \quad (6)$$

where θ_V and ψ_V are Voigt rotation angle and ellipticity, respectively. If the substrate has a relatively small refractive index ($n_s \rightarrow 1$), the SH angle will be much larger than the Voigt angle, indicating that the optical detection upon reflection is more suitable than upon transmission for studying the second-order magneto-optical effects of magnetic thin films.

TABLE I. Magnetic space groups of monolayer MPS_3 with different magnetic orders. The magnetization directions are labeled in brackets. The symbol \checkmark (\times) indicates the in-plane optical anisotropy (isotropy). The dipole selection rules at some high-symmetry points (e.g., Γ and K) are listed.

Magnetic orders	Magnetic space group	In-plane anisotropy ($\sigma_{xx} \neq \sigma_{yy}$)	Dipole Sele. rules ($\mathbf{E} \perp z$)
FM (x)	$C2'/m'$	\checkmark	$\Gamma_2^+ \leftrightarrow \Gamma_2^-$
FM (z)	$P\bar{3}1m'$	\times	$\Gamma_4^+ \leftrightarrow \Gamma_5^-, \Gamma_6^-$ $K_4 \leftrightarrow K_5$ $\Gamma_5^+ \leftrightarrow \Gamma_4^-, \Gamma_6^-$ $K_4 \leftrightarrow K_6$ $\Gamma_6^+ \leftrightarrow \Gamma_4^-, \Gamma_5^-$ $K_5 \leftrightarrow K_6$
Néel-AFM (x)	$C2'/m$	\checkmark	$\Gamma_3\Gamma_4 \leftrightarrow \Gamma_3\Gamma_4$
Néel-AFM (z)	$P\bar{3}1m$	\times	$\Gamma_4 \leftrightarrow \Gamma_4$ $K_4 \leftrightarrow K_4$ $\Gamma_4 \leftrightarrow \Gamma_5\Gamma_6$ $K_4 \leftrightarrow K_5K_6$
zigzag-AFM (x,z)	P_c2_1/m	\checkmark	$\Gamma_3^+\Gamma_4^+ \leftrightarrow \Gamma_3^-\Gamma_4^-$
stripy-AFM (x,z)	P_a2_1/c	\checkmark	$\Gamma_3^+\Gamma_4^+ \leftrightarrow \Gamma_3^-\Gamma_4^-$

The complex SH angle (see Eq. (5)) can also be written in terms of optical conductivity using the relationship between permittivity and optical conductivity, given by, $\epsilon_{\mu\nu} = \delta_{\mu\nu} + \frac{4\pi i}{\omega} \sigma_{\mu\nu}$. The off-diagonal elements of the optical conductivity containing the z -component (e.g., σ_{yz}) have to be zero due to the 2D nature of our considered systems. This can be read from Eq. (8) since the quenched electron velocity along the z direction ($\hat{v}_z = 0$) leads to the vanishing σ_{yz} and σ_{zx} . Therefore, the complex SH angle is simply expressed as

$$\theta_{SH} + i\psi_{SH} \approx \frac{4\pi d}{c(n_s^2 - 1)}(\sigma_{yy} - \sigma_{xx}), \quad (7)$$

which is the formula implemented in our first-principles calculations. The 2D vdW magnetic materials are often grown on transparent substrates, such as SiO_2 , whose refractive index n_s is a real number. In this case, the SH rotation angle and ellipticity are determined by the real and imaginary parts of conductivity anisotropy (i.e., $\sigma_{yy} - \sigma_{xx}$), respectively. On account of this relationship, the conductivity anisotropy can be accurately measured by MOSHE spectroscopy.

For monolayer MPS_3 , the transition metal atoms M form a flat honeycomb lattice and a bipyramid of P_2S_6 ligand locates at the center of hexagon (Fig. 2a,b). If removing the magnetic orders, monolayer MPS_3 is in-plane isotropic due to its crystallographic point group of D_{3d} . Nevertheless, the honeycomb lattice can host a variety of magnetic orders, including FM state as well as Néel-, zigzag-, and stripy-AFM states (Fig. 2c-e) [31], depending on the relative strength of intralayer first, second, and third nearest-neighbour exchange interactions. $MnPS_3$ displays the Néel-AFM order with the out-of-plane (z -axis) magnetic easy axis [17]. $FePS_3$ and $NiPS_3$ display the zigzag-AFM order with the out-of-plane (z -axis) [18] and in-plane (x -axis) [32] magnetization, respectively. The exfoliated atomic layers persist long-range AFM orders down to bilayer or even monolayer limit, and their magnetic critical temperatures are nearly independent on thickness. Moreover, the magnetization for Néel- and zigzag-AFM

states can be tuned between the out-of-plane and in-plane directions via atomic substitution [33], and the FM state was predicted to be their ground states under sufficient large carrier density [34].

Before practically calculating MOSHE, we conduct symmetry analysis to evaluate which magnetic order breaks the in-plane optical isotropy of monolayer MPS_3 . The magnetic space groups computed by ISOTROPY code [35] are listed in Table I, in which the shapes of optical conductivity tensors are identified by SYMMETR code [36, 37]. As expected, all of the magnetic orders with the magnetization along the x -axis are in-plane anisotropic, which allows the MOSHE. For FM and Néel-AFM orders with the spins along the z -axis, the in-plane

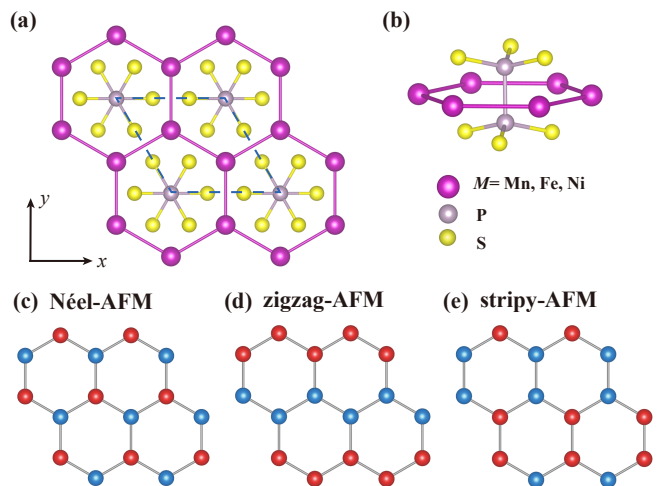


FIG. 2. (a,b) Top and side views of monolayer MPS_3 . Blue dashed lines draw out the primitive cell of non-magnetic state. (c-e) The Néel-, zigzag-, and stripy-antiferromagnetic orders on a honeycomb lattice. Red and blue spheres represent the M atoms with opposite directions of spin magnetic moments.

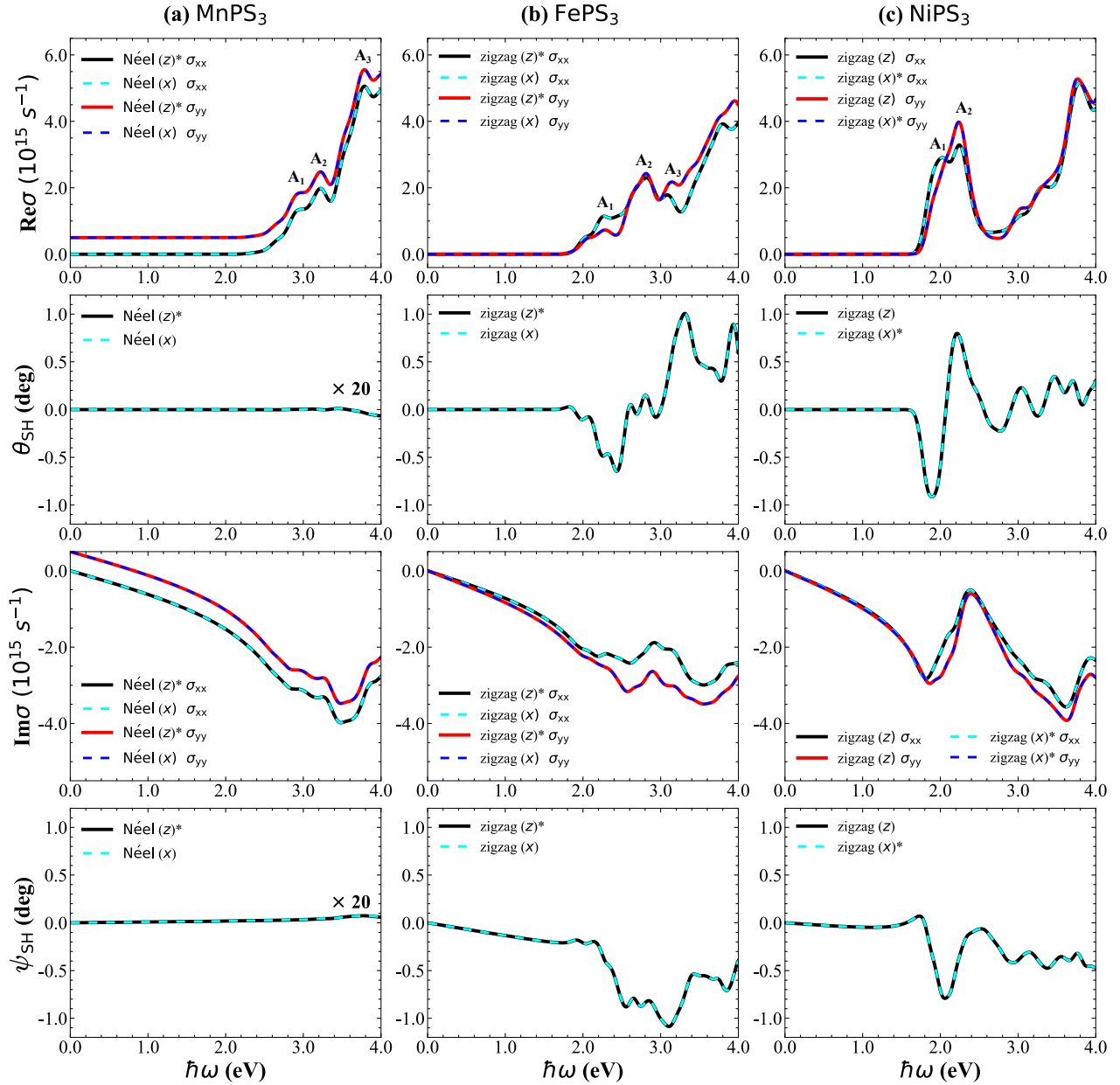


FIG. 3. Optical conductivities and MOSHE spectra of monolayer (a) MnPS_3 , (b) FePS_3 , and (c) NiPS_3 on SiO_2 substrate. The panels from top to bottom show the real part of optical conductivity ($\text{Re}\sigma$), SH rotation angle (θ_{SH}), imaginary part of optical conductivity ($\text{Im}\sigma$), and SH ellipticity (ψ_{SH}), respectively. The magnetization direction of each magnetic order is indicated in brackets, and an asterisk labels the ground state. The $\text{Re}\sigma_{yy}$ and $\text{Im}\sigma_{yy}$ of MnPS_3 are moved upward by $0.5 \times 10^{15} \text{s}^{-1}$ for a clear observation, and the θ_{SH} and ψ_{SH} of MnPS_3 are multiplied by a factor of 20. A_1 , A_2 , and A_3 mark several absorption peaks of $\text{Re}\sigma$ in the low-energy range.

isotropy is preserved by the three-fold rotational symmetry in magnetic space groups of $P\bar{3}1m'$ and $P\bar{3}1m$, respectively. The magnetic space groups of zigzag- and stripy-AFM orders with the magnetization along the z -axis are the same as that along the x -axis, such that the z -axis magnetization is also in-plane anisotropic and may also lead to the MOSHE. According to the mirror symmetry \mathcal{M}_y in the zigzag-AFM order, the orthogonal anisotropic axes are determined to be the x - and y -axes as shown in Fig. 2.

Figure 3 plots the calculated optical conductivities and MOSHE spectra of monolayer AFM MPS_3 . We first discuss the results of each material on its magnetic ground state. For MnPS_3 with the z -axis Néel-AFM order (Fig. 3a), the spectrum of σ_{xx} is identical to that of σ_{yy} , which is governed by the in-plane optical isotropy, and the resulting SH rotation angle (θ_{SH}) and SH ellipticity (ψ_{SH}) are negligibly small. The absorptive parts of optical conductivity tensor, $\text{Re}\sigma_{xx}$ and $\text{Re}\sigma_{yy}$, are determined by the symmetry-allowed dipole se-

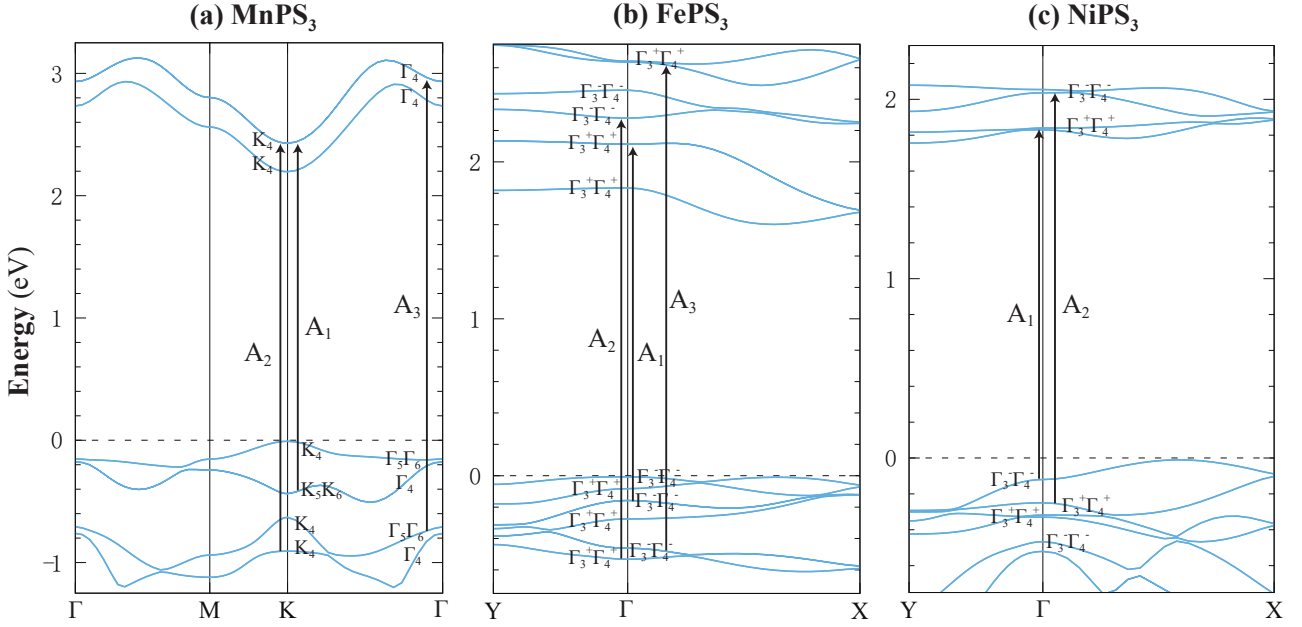


FIG. 4. Relativistic band structures of monolayer (a) MnPS_3 with the z -axis Néel-AFM order, (b) FePS_3 with the z -axis zigzag-AFM order, and (c) NiPS_3 with the x -axis zigzag-AFM order. The irreducible representations of relevant bands at the Γ and K points are labeled. The principal interband transitions A_1 , A_2 , and A_3 are indicated by arrows, corresponding to the peaks of $\text{Re}\sigma_{xx}$ and $\text{Re}\sigma_{yy}$ in Fig. 3.

lection rules listed in Table I, from which one can analyze the origination of main peaks in conductivity spectra. For example, the A_1 and A_2 peaks at the energies of 2.9 eV and 3.2 eV originate from the interband transitions $K_5K_6 \rightarrow K_4$ and $K_4 \rightarrow K_4$ at the K -point, respectively, and the A_3 peak at the energy of 3.7 eV originates from the interband transition $\Gamma_5\Gamma_6 \rightarrow \Gamma_4$ at the Γ -point, as depicted in Fig. 4a. For FePS_3 with the z -axis zigzag-AFM order (Fig. 3b), one can discern a clear anisotropy in real and imaginary parts of optical conductivity above the absorption edge (~ 1.8 eV). The spectra of $\text{Re}\sigma_{xx}$ and $\text{Re}\sigma_{yy}$ feature three peaks of A_1 , A_2 , and A_3 at the energies of 2.3 eV, 2.8 eV, and 3.1 eV, respectively, which come from the interband transitions between the $\Gamma_3^+\Gamma_4^+$ and $\Gamma_3^-\Gamma_4^-$ states at the Γ -point (Fig. 4b). The obvious difference in values between $\text{Re}\sigma_{xx}$ and $\text{Re}\sigma_{yy}$ around the A_1 and A_3 peaks generate the maximal SH rotation angles of -0.7° at 2.4 eV and of 1.0° at 3.3 eV, respectively. The SH ellipticity is always negative and reaches up to -1.1° at 3.1 eV. For NiPS_3 with the x -axis zigzag-AFM order (Fig. 3c), the real part of optical conductivity resembles the experimental detection of its bulk crystal [38]. Both $\text{Re}\sigma_{xx}$ and $\text{Re}\sigma_{yy}$ spectra show the A_2 peak at 2.3 eV due to the interband transition $\Gamma_3^+\Gamma_4^+ \rightarrow \Gamma_3^-\Gamma_4^-$, while an additional peak A_1 appears at 2.0 eV for $\text{Re}\sigma_{xx}$ which is related to the transition from the $\Gamma_3^-\Gamma_4^-$ state (highest valence band) to the $\Gamma_3^+\Gamma_4^+$ state (lowest conduction band) at the Γ -point (Fig. 4c). In the energy range of $1.7 \sim 2.5$ eV, the significant anisotropy of optical conductivity has to result in large SH rotation angles, e.g., -0.9° at 1.9 eV and 0.8° at 2.2 eV. The corresponding SH ellipticity is also obviously large with a peak of -0.8° at 2.1 eV.

Of particular interest here is that the optical conductivity

spectra are almost not changed when the magnetization direction changes from the z -axis to the x -axis or vice versa (Fig. 3). This is very similar to the cases of three-dimensional noncollinear AFM Mn_3X ($X = \text{Rh}, \text{Ir}, \text{Pt}$) [39] and 2D vdW FM Fe_nGeTe_2 ($n = 3, 4, 5$) [40]. It can be easily understood as the longitudinal optical conductivities (σ_{xx} and σ_{yy}) are closely related to the joint density of states and interband transition probability [41] which are basically not influenced when the angle between adjacent spins keeps fixed. It follows that the SH spectra of MPS_3 are insensitive to magnetization direction, e.g., FePS_3 and NiPS_3 with the z - and x -axes zigzag-AFM orders (Fig. 3b,c). In the case of MnPS_3 with the x -axis Néel-AFM order, the optical conductivities are identical to the results of z -axis Néel-AFM order, such that the SH rotation angle and ellipticity are also negligibly small (Fig. 3a), even though the appearance of MOSHE with the x -axis Néel-AFM order is allowed by symmetry (Table I). Similarly, since the z -axis FM order exhibits in-plane isotropy, the MOSHE in all the three materials with the x -axis FM order are rather small (see Supplementary Fig. 1), e.g., the largest SH rotation angle (appearing in FePS_3) is only 0.05° . Therefore, we suggest that it is more likely to observe large second-order magneto-optical effects in AFM materials that exhibit in-plane anisotropy when the spins are out-of-plane oriented, such as the MPS_3 family with the zigzag-AFM and stripy-AFM (Fig. 3b,c) orders (see Supplementary Fig. 2).

Next, we move on to discuss the MOSHE in bilayer FePS_3 and NiPS_3 on their magnetic ground states. For FePS_3 , two types of interlayer magnetic structures have long been reported. One is the zigzag-AFM chain along the x -axis (type-A) with AFM interlayer coupling (Fig. 5a) [42], while the

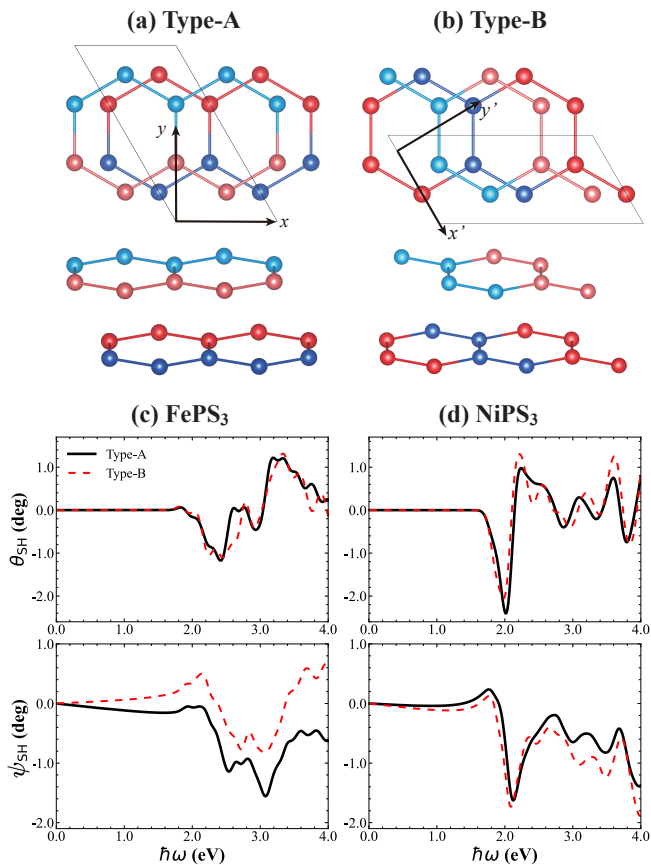


FIG. 5. (a,b) Two types of magnetic structures for bilayer MPS_3 with the zigzag-AFM chains along the x and x' -axes. Bright (dark) red and blue spheres denote the M atoms on bottom (top) layer with opposite spin magnetic moments, whereas P and S atoms are not shown. The solid black lines draw out the 2D primitive cell. (c,d) Magneto-optical Schaefer-Hubert spectra (θ_{SH} and ψ_{SH}) of bilayer $FePS_3$ and $NiPS_3$ with the type-A and type-B magnetic structures.

other one is the zigzag-AFM chain along the x' -axis (type-B) with FM interlayer coupling (Fig. 5b) [43]. Recently, the coexistence of the two types of magnetic structures in multilayer $FePS_3$ has been confirmed by combining MLD and second-harmonic generation measurements [21]. For $NiPS_3$ powder and single crystal, as far as we know, only the type-A zigzag chain with FM interlayer coupling has been reported [44, 45]. We speculate that the type-B structure may also exist in bilayer and multilayer $NiPS_3$.

Here we consider both FM and AFM interlayer coupling for type-A and type-B zigzag chains in bilayer $FePS_3$ and $NiPS_3$. The optical conductivities are not shown because they retain the overall trend in monolayers (Fig. 3b,c) with slightly change in magnitudes due to the weak interlayer vdW interactions. The calculated SH spectra are plotted in Fig. 5c,d, in which the interlayer FM and AFM coupling are not labeled since their spectra are identical to each other. One can observe that for both $FePS_3$ and $NiPS_3$, the profiles of SH rotation angles for two types of zigzag chains resemble to each other (top panels of Fig. 5c,d). Moreover, the SH rotation an-

gles for monolayers and bilayers are also similar in the sense that their peaks appear at almost the same photon energy. The calculated SH rotation angles of bilayer $FePS_3$ ($NiPS_3$) are surprisingly large recording to -1.2° at 2.4 eV and 1.2° at 3.2 eV (-2.4° at 2.0 eV and 1.0° at 2.2 eV). In contrast to the SH rotation angles, the SH ellipticities are highly correlated to the zigzag chain structures (bottom panels of Fig. 5c,d). The ellipticity spectra of bilayer $FePS_3$ with type-A and type-B structures show a striking contrast in a wide range of photon energy, in particular at 2.4 eV and 3.4 eV where ψ_{SH} for type-B structure are zero. As well, there is significant difference between the type-A and type-B structures of bilayer $NiPS_3$ from 3.0 eV to 3.7 eV. We suggest that the dramatic features in SH ellipticity can be used to distinguish the magnetic structures of bilayer MPS_3 .

In summary, our work establishes a simple theoretical framework for studying the magneto-optical Schaefer-Hubert effect in 2D magnetic materials using first-principles calculations, and also proposes second-order magneto-optical spectroscopy to be a powerful technique for accurately detecting the in-plane anisotropy in various magnetic structures. The calculated results demonstrate that monolayer $FePS_3$ and $NiPS_3$ with the zigzag antiferromagnetic order exhibit large Schaefer-Hubert angles (up to 1°) in visible light and near-ultraviolet range. We further find that the Schaefer-Hubert effect is interestingly insensitive to the orientations of Néel vector. Finally, the magneto-optical response for bilayer $FePS_3$ and $NiPS_3$ with different stackings of zigzag antiferromagnetic chains are studied. Surprisingly, the Schaefer-Hubert angle of bilayer $NiPS_3$ records up to 2.4° , and the obvious discrepancy in ellipticity spectra enable a distinction of different interlayer magnetic structures. The excellent properties render MPS_3 family a novel AFM materials platform for nanophotonic devices. More importantly, our theoretical framework allows for high-throughput study of Schaefer-Hubert effect among 2D AFM materials for finding potentially interesting systems.

METHODS

First-principles calculations

The electronic structure calculations were performed using the projector augmented wave (PAW) method [46], implemented in Vienna *ab initio* Simulation Package (VASP) [47]. The exchange-correlation effects were treated using the generalized gradient approximation with the Perdew-Burke-Ernzerhof (GGA-PBE) parameterization [48]. The cutoff energy was set to 300 eV and the energy convergence criterion was chosen to 10^{-6} eV. A k -mesh of $12 \times 12 \times 1$ ($12 \times 6 \times 1$) was used for the 1×1 (1×2) unit cell. Spin-orbit coupling (SOC) effect was included in our calculations. The correlation effects of the d -orbitals of Fe, Ni, and Mn atoms were treated by the GGA+U method [49], and the effective Hubbard parameters were set to 3.0 eV, 4.0 eV, and 5.0 eV, respectively. The experimental lattice constants are adopted for $MnPS_3$ (6.077 Å), $FePS_3$ (5.947 Å), and $NiPS_3$ (5.812 Å) [50]. The van der Waals interactions were considered using the DFT-D2 method [51]. A vacuum layer of 15 Å was used to eliminate the interactions between the adjacent atomic layers.

Magneto-optical Schäfer-Hubert effect

The complex Schäfer-Hubert angle in two-dimensional (2D) materials were computed according to Eq. (7). We constructed the maximally-localized Wannier functions, including the d -orbitals of Mn, Fe, and Ni atoms, the s - and p -orbitals of P atoms, and the p -orbitals of S atoms, using WANNIER90 package [52]. Then the optical conductivity was calculated using the Kubo-Greenwood formula [53],

$$\sigma_{\mu\nu} = \frac{ie^2\hbar}{N_k V} \sum_{\mathbf{k}} \sum_{n,m} \frac{f_{m\mathbf{k}} - f_{n\mathbf{k}}}{E_{m\mathbf{k}} - E_{n\mathbf{k}}} \times \frac{\langle \psi_{n\mathbf{k}} | \hat{v}_\mu | \psi_{m\mathbf{k}} \rangle \langle \psi_{m\mathbf{k}} | \hat{v}_\nu | \psi_{n\mathbf{k}} \rangle}{E_{m\mathbf{k}} - E_{n\mathbf{k}} - (\hbar\omega + i\eta)}, \quad (8)$$

where $f_{n\mathbf{k}}$, V , N_k , ω , and η are the Fermi-Dirac distribution function, volume of unit cell, total number of k -points in the Brillouin zone, photon frequency, and energy smearing parameter, respectively. $\hat{v}_{\mu(\nu)}$ is velocity operator with subscripts $\mu, \nu \in \{x, y, z\}$ denotes Cartesian components. $\psi_{n\mathbf{k}}$ and $E_{n\mathbf{k}}$ are the Wannier functions and interpolated energy at the band index n and momentum \mathbf{k} , respectively. A k -mesh of $400 \times 400 \times 1$ was used to converge the optical conductivity and η was set to be 0.1 eV. The effective thicknesses (d) of MnPS₃, FePS₃, and NiPS₃ monolayers were taken from the interlayer distances of their bulk compounds, that is, 6.796 Å, 6.722 Å, and 6.632 Å, respectively [43]. The experimental refractive index of SiO₂ at different photon energies [54] was acquired from an online database (<https://refractiveindex.info>).

Dipole selection rules

The characters of the energy bands at high-symmetry k -points were determined using MagVasp2trace code [55, 56]. The corresponding irreducible corepresentations and dipole selection rules were identified by MSGCorep package [57, 58]. Here, we take the magnetic space group $P3'1m$ as an example to illustrate how to find out the dipole selection rules. For an in-plane polarized light (i.e., $\mathbf{E} \perp z$), the dipole operators are defined by either $-e\hat{x}$ or $-e\hat{y}$, which together transform as the bases of the irreducible corepresentation Γ_3 of the group $P3'1m$. Using the command "showMSGCorepDirectProduct" in MSGCorep package, we can obtain the direct products and their decompositions between Γ_3 and other corepresentations (Supplementary Fig. 3). It is easy to find that the dipole selection rules are $\Gamma_4 \leftrightarrow \Gamma_4$ and $\Gamma_4 \leftrightarrow \Gamma_5\Gamma_6$.

DATA AVAILABILITY

The data that support the findings of this study are available from the corresponding author on reasonable request.

CODE AVAILABILITY

The codes that are necessary to reproduce the findings of this study are available from the corresponding author on reasonable request.

REFERENCES

1. Gong, C. *et al.* Discovery of intrinsic ferromagnetism in two-dimensional van der Waals crystals. *Nature* **546**, 265 (2017).
2. Huang, B. *et al.* Layer-dependent ferromagnetism in a van der

3. Huang, B. *et al.* Electrical control of 2D magnetism in bilayer CrI₃. *Nat. Nanotechnol.* **13**, 544 (2018).
4. Yang, B., Zhang, X., Yang, H., Han, X. & Yan, Y. Strain controlling transport properties of heterostructure composed of monolayer CrI₃. *Appl. Phys. Lett.* **114**, 192405 (2019).
5. Huang, B. *et al.* Emergent phenomena and proximity effects in two-dimensional magnets and heterostructures. *Nat. Mater.* **19**, 1276 (2020).
6. Katayama, T., Suzuki, Y., Awano, H., Nishihara, Y. & Koshizuka, N. Enhancement of the magneto-optical Kerr rotation in Fe/Cu bilayered films. *Phys. Rev. Lett.* **60**, 1426 (1988).
7. Suzuki, Y., Katayama, T., Yoshida, S., Tanaka, K. & Sato, K. New magneto-optical transition in ultrathin Fe(100) films. *Phys. Rev. Lett.* **68**, 3355 (1992).
8. Feng, W., Guo, G.-Y. & Yao, Y. Tunable magneto-optical effects in hole-doped group-IIIa metal-monochalcogenide monolayers. *2D Mater.* **4**, 015017 (2017).
9. Zhou, X., Feng, W., Li, F. & Yao, Y. Large magneto-optical effects in hole-doped blue phosphorene and gray arsenene. *Nanoscale* **9**, 17405 (2017).
10. Fang, Y., Wu, S., Zhu, Z.-Z. & Guo, G.-Y. Large magneto-optical effects and magnetic anisotropy energy in two-dimensional Cr₂Ge₂Te₆. *Phys. Rev. B* **98**, 125416 (2018).
11. Gudelli, V. K. & Guo, G.-Y. Magnetism and magneto-optical effects in bulk and few-layer CrI₃: a theoretical GGA + U study. *New J. Phys.* **21**, 053012 (2019).
12. Saidl, V. *et al.* Optical determination of the Néel vector in a CuMnAs thin-film antiferromagnet. *Nat. Photon.* **11**, 91 (2017).
13. Zheng, Z. *et al.* Magneto-optical probe of ultrafast spin dynamics in antiferromagnetic CoO thin films. *Phys. Rev. B* **98**, 134409 (2018).
14. Grigorev, V. *et al.* Optical readout of the Néel vector in the metallic antiferromagnet Mn₂Au. *Phys. Rev. Appl.* **16**, 014037 (2021).
15. Voigt, W. *Magneto-und Elektrooptik* (Leipzig, B. G. Teubner, 1908).
16. Schäfer, R. & Hubert, A. A new magneto-optic effect related to non-uniform magnetization on the surface of a ferromagnet. *Phys. Stat. Sol. (a)* **118**, 271 (1990).
17. Kim, K. *et al.* Antiferromagnetic ordering in van der Waals 2D magnetic material MnPS₃ probed by raman spectroscopy. *2D Mater.* **6**, 041001 (2019).
18. Lee, J.-U. *et al.* Ising-type magnetic ordering in atomically thin FePS₃. *Nano Lett.* **16**, 7433 (2016).
19. Lançon, D., Ewings, R. A., Guidi, T., Formisano, F. & Wildes, A. R. Magnetic exchange parameters and anisotropy of the quasi-two-dimensional antiferromagnet NiPS₃. *Phys. Rev. B* **98**, 134414 (2018).
20. Zhang, Q. *et al.* Observation of giant optical linear dichroism in a zigzag antiferromagnet FePS₃. *Nano Lett.* **21**, 6938 (2021).
21. Ni, Z., Huang, N., Haglund, A. V., Mandrus, D. G. & Wu, L. Observation of giant surface second-harmonic generation coupled to nematic orders in the van der Waals antiferromagnet FePS₃. *Nano Lett.* **22**, 3283 (2022).
22. Zhang, X.-X. *et al.* Spin dynamics slowdown near the antiferromagnetic critical point in atomically thin FePS₃. *Nano Lett.* **21**, 5045 (2021).
23. Zhang, H. *et al.* Cavity-enhanced linear dichroism in a van der Waals antiferromagnet. *Nat. Photonics* **16**, 311 (2022).
24. Yuan, H. *et al.* Polarization-sensitive broadband photodetector using a black phosphorus vertical p-n junction. *Nat. Nanotechnol.* **10**, 707 (2015).

25. Biswas, S., Grajower, M. Y., Watanabe, K., Taniguchi, T. & Atwater, H. A. Broadband electro-optic polarization conversion with atomically thin black phosphorus. *Science* **374**, 448 (2021).
26. Wang, X. *et al.* Short-wave near-infrared linear dichroism of two-dimensional germanium selenide. *J. Am. Chem. Soc.* **139**, 14976 (2017).
27. Wang, X. *et al.* Spin-induced linear polarization of photoluminescence in antiferromagnetic van der Waals crystals. *Nat. Mater.* **20**, 964 (2021).
28. Ni, Z. *et al.* Imaging the Néel vector switching in the monolayer antiferromagnet MnPSe₃ with strain-controlled Ising order. *Nat. Nanotechnol.* **16**, 782 (2021).
29. Zvezdin, A. K. & Kotov, V. A. *Modern Magnetooptics and Magneto-optical Materials* (Institute of Physics Publishing, Bristol and Philadelphia, 1997).
30. Mertins, H. C. *et al.* Observation of the X-ray magneto-optical Voigt effect. *Phys. Rev. Lett.* **87**, 047401 (2001).
31. Sivasdas, N., Daniels, M. W., Swendsen, R. H., Okamoto, S. & Xiao, D. Magnetic ground state of semiconducting transition-metal trichalcogenide monolayers. *Phys. Rev. B* **91**, 235425 (2015).
32. Kim, K. *et al.* Suppression of magnetic ordering in XXZ-type antiferromagnetic monolayer NiPS₃. *Nat. Commun.* **10**, 345 (2019).
33. Basnet, R. *et al.* Controlling magnetic exchange and anisotropy by nonmagnetic ligand substitution in layered MPX₃ (M = Ni, Mn; X = S, Se). *Phys. Rev. Res.* **4**, 023256 (2022).
34. Chittari, B. L. *et al.* Electronic and magnetic properties of single-layer MPX₃ metal phosphorous trichalcogenides. *Phys. Rev. B* **94**, 184428 (2016).
35. Stokes, H. T., Hatch, D. M. & Campbell, B. J. Isotropy software suite. <https://stokes.byu.edu/iso/isotropy.php>
36. Železný, J. *et al.* Spin-orbit torques in locally and globally non-centrosymmetric crystals: antiferromagnets and ferromagnets. *Phys. Rev. B* **95**, 014403 (2017).
37. A code for analyzing the shape of linear response tensors. <https://bitbucket.org/zeleznyj/linear-response-symmetry>
38. Kim, S. Y. *et al.* Charge-spin correlation in van der Waals antiferromagnet NiPS₃. *Phys. Rev. Lett.* **120**, 136402 (2018).
39. Feng, W., Guo, G.-Y., Zhou, J., Yao, Y. & Niu, Q. Large magneto-optical kerr effect in noncollinear antiferromagnets Mn₃X (X = Rh, Ir, Pt). *Phys. Rev. B* **92**, 144426 (2015).
40. Yang, X., Zhou, X., Feng, W. & Yao, Y. Strong magneto-optical effect and anomalous transport in the two-dimensional van der Waals magnets Fe_nGeTe₂ (n = 3, 4, 5). *Phys. Rev. B* **104**, 104427 (2021).
41. Stroppa, A., Picozzi, S., Continenza, A., Kim, M. & Freeman, A. J. Magneto-optical properties of (Ga,Mn)As: an *ab initio* determination. *Phys. Rev. B* **77**, 035208 (2008).
42. Kurosawa, K., Saito, S. & Yamaguchi, Y. Neutron diffraction study on MnPS₃ and FePS₃. *J. Phys. Soc. Jpn.* **52**, 3919 (1983).
43. Le Flem, G., Brec, R., Ouvard, G., Louisy, A. & Segransan, P. Magnetic interactions in the layer compounds MPX₃ (M = Mn, Fe, Ni; X = S, Se). *J. Phys. Chem. Solids* **43**, 455 (1982).
44. Brec, R. Review on structural and chemical properties of transition metal phosphorous trisulfides MPS₃. *Solid State Ionics* **22**, 3 (1986).
45. Wildes, A. R. *et al.* Magnetic structure of the quasi-two-dimensional antiferromagnet NiPS₃. *Phys. Rev. B* **92**, 224408 (2015).
46. Blöchl, P. E. Projector augmented-wave method. *Phys. Rev. B* **50**, 17953 (1994).
47. Kresse, G. & Joubert, D. From ultrasoft pseudopotentials to the projector augmented-wave method. *Phys. Rev. B* **59**, 1758 (1999).
48. Perdew, J. P., Burke, K. & Ernzerhof, M. Generalized gradient approximation made simple. *Phys. Rev. Lett.* **77**, 3865 (1996).
49. Dudarev, S. L., Botton, G. A., Savrasov, S. Y., Humphreys, C. J. & Sutton, A. P. Electron-energy-loss spectra and the structural stability of nickel oxide: an LSDA+U study. *Phys. Rev. B* **57**, 1505 (1998).
50. Ouvard, G., Brec, R. & Rouxel, J. Structural determination of some MPS₃ layered phases (M = Mn, Fe, Co, Ni and Cd). *Mater. Res. Bull.* **20**, 1181 (1985).
51. Grimme, S. Semiempirical GGA-type density functional constructed with a long-range dispersion correction. *J. Comput. Chem.* **27**, 1787 (2006).
52. Pizzi, G. *et al.* Wannier90 as a community code: new features and applications. *J. Phys.: Condens. Matter* **32**, 165902 (2020).
53. Yates, J. R., Wang, X., Vanderbilt, D. & Souza, I. Spectral and fermi surface properties from Wannier interpolation. *Phys. Rev. B* **75**, 195121 (2007).
54. Ghosh, G. Dispersion-equation coefficients for the refractive index and birefringence of calcite and quartz crystals. *Opt. Commun.* **163**, 95 (1999).
55. Xu, Y. *et al.* High-throughput calculations of magnetic topological materials. *Nature* **586**, 702 (2020).
56. Elcoro, L. *et al.* Magnetic topological quantum chemistry. *Nat. Commun.* **12**, 5965 (2021).
57. Liu, G.-B., Chu, M., Zhang, Z., Yu, Z.-M. & Yao, Y. Spacegroupirep: a package for irreducible representations of space group. *Comput. Phys. Commun.* **265**, 107993 (2021).
58. Liu, G.-B., Zhang, Z., Yu, Z.-M. & Yao, Y. Msgcorep: a package for corepresentations of magnetic space groups. Preprint at <https://arxiv.org/abs/2211.10740> (2022)

ACKNOWLEDGEMENTS

The authors thank Shifeng Qian and Run-Wu Zhang for helpful discussion. This work is supported by the National Key R&D Program of China (Grant Nos. 2022YFA1402600, 2022YFA1403800, and 2020YFA0308800), the National Natural Science Foundation of China (Grant Nos. 12274027, 11874085, 12274028, and 12061131002), the Science & Technology Innovation Program of Beijing Institute of Technology (Grant No. 2021CX01020), and the Sino-German Mobility Programme (Grant No. M-0142).

COMPETING INTERESTS

The authors declare no competing interests.

AUTHOR CONTRIBUTIONS

W.F. and Y.Y. conceived the research. P.Y. derived the formula and performed the first-principles calculations. P.Y. and G.-B.L. carried out the symmetry analysis. P.Y. and W.F. wrote the manuscript with discussion from all authors

ADDITIONAL INFORMATION

Supplementary information is available for this paper at <https://doi.org/xxxxxx>.

Correspondence and requests for materials should be addressed to W.F.

Reprints and permission information is available at

<http://www.nature.com/reprints>

Publisher's note Springer Nature remains neutral with regard

to jurisdictional claims in published maps and institutional affiliations.